




## Probing conducting interfaces by combined photoluminescence and transport measurements: LaVO<sub>3</sub> and SrTiO<sub>3</sub> interface as a case study

Anamika Kumari <sup>1</sup>, Joydip De <sup>2</sup>, Sushanta Dattagupta,<sup>3</sup> Hirendra N. Ghosh,<sup>4</sup> Santanu Kumar Pal <sup>2</sup> and S. Chakraverty<sup>1,\*</sup>

<sup>1</sup>Quantum Materials and Devices Unit, Institute of Nano Science and Technology, Sector-81, Punjab 140306, India

<sup>2</sup>Indian Institute of Science Education and Research Mohali, Knowledge City, Sector-81, SAS Nagar, Manauli 140306, India

<sup>3</sup>Bose Institute, P-1/12, CIT Road, Scheme VIII, Kankurgachi, Kolkata, West Bengal-700054, India

<sup>4</sup>Institute of Nano Science and Technology, Sector-81, Punjab 140306, India



(Received 11 January 2021; accepted 28 July 2021; published 23 August 2021)

The carrier-density distribution near a conducting interface and the related band structure are topics of great contemporary importance in low-dimensional quantum solids. We propose a scheme, innovatively combining the spectroscopy techniques of photoluminescence and time-correlated single-photon counting with transport measurements of resistivity to unravel the carrier distribution, the shape of quantum well, energy subbands, and Fermi surfaces of the conducting interface of LaVO<sub>3</sub> and SrTiO<sub>3</sub>. Electronic parameters, such as the carrier density, the mobility, estimated from the electrical measurements, are in remarkably good agreement with those extracted from the spectroscopy with theoretical modeling providing a bridge between the two sets of data analysis.

DOI: [10.1103/PhysRevB.104.L081111](https://doi.org/10.1103/PhysRevB.104.L081111)

A “two-dimensional electron gas” (2DEG) is a model system that consists of non(weakly) interacting highly conducting electrons that can freely move in two dimensions but confined in the third dimension. The 2DEG is of common occurrence in a transistor made out of semiconductors, specifically metal-oxide-semiconductor-field-effect transistors (MOSFETs) [1]. Electrons confined in a quantum well at the heterojunction of two semiconducting materials also act as a 2DEG at the interface [2]. Such a 2DEG exhibits higher mobilities than those in MOSFETs. The heterojunction-based 2DEGs are interesting not only because of their fascinating physical properties, but also because of their potential applications to modern electronics industries [3–5].

Perovskite oxides could turn out to be an interesting replacement of the conventional semiconductors because of their emergent properties, such as superconductivity [6,7], magnetism [8], coexisting magnetism and superconductivity [9], optically induced ferroelectricity [10], multiferroicity [11,12], persistent photocurrent [13–15], photoinduced demagnetization and metal insulator transition [16], Rashba spin splitting [17], Shubnikov–de Hass oscillations [18], to name a few. These functionalities, coupled with 2DEG behavior may offer a new pathway for the realization of integrated laboratory-on-chip devices [19,20]. In a pioneering paper, Ohtomo and Hwang demonstrated the appearance of a high mobility two-dimensional conducting layer at the interface of two band insulators LaAlO<sub>3</sub> (LAO) and SrTiO<sub>3</sub> (STO) [3]. Such interfaces, subsequently, showed further interesting properties, although many fundamental questions remain unresolved to this date. The origin of conductivity at the interface

is explained by a number of proposed mechanisms, such as polar catastrophe or electronic reconstruction, cation intermixing, oxygen vacancies, and cation stoichiometry. None of the mechanisms is fully accepted so far, and the origin of this 2DEG at the interface of insulating oxides is still in debate [21,22].

Among all the proposed models the most accepted one is the polar catastrophe model. For a perovskite oxide ABO<sub>3</sub>, the atomic stacking consists of AO and BO<sub>2</sub> layers in the (001) direction. These layers could either be charged neutral as in STO [(SrO) = 0 and (TiO<sub>2</sub>) = 0] or could be charged +1/−1, alternatively, as in LAO [(LaO) = +1 and (AlO<sub>2</sub>) = −1]. When two such perovskites are stuck together, a polar discontinuity at the interface occurs, and a diverging electrostatic potential builds up. This diverging potential can be avoided by a transfer of (0.5-electron) charge to the interface. This is known as the polar catastrophe model. This model has two important consequences: (1) A critical thickness of the film is needed to realize the conducting interface, and (2) the interface should be doped with half an electron per unit cell. It is reported that for the LAO/STO interface, although a critical thickness is needed to realize the conducting interface, the interfacial carrier concentration is much less than that predicted from the model. However, in the case of the GTO/STO (GTO: GdTiO<sub>3</sub>) heterostructure the interface is doped 0.5 electron per unit cell as predicted by polar catastrophe model but does not need any critical thickness of GTO to get interfacial conductivity. Whereas, the LVO/STO interface satisfies both the characteristics of polar catastrophe model, it needs a critical thickness of LVO to realize the conducting interface, and the interface is doped with 0.5 electron per unit cell. The *n*-type interface in LAO/STO is a heterostructure of two band insulators, whereas both LVO and GTO are Mott insulators. It is important to note that LVO(GTO)

\*suvankar.chakraverty@gmail.com

is a  $d^2(d^1)$  system whereas LAO is a  $d^0$  system. Despite that it is interesting to note that the orbital characters of the interfacial electron for all these three heterostructures predominantly have  $xy$  characters. On the other hand, that within the STO substrate, it is predominantly of the  $yz/xz$  character for all these heterostructures [23,24]. In addition, the growth condition of the LAO thin film is rather reducing (typically 750 °C) compared to LVO (typically 600 °C). Furthermore, Al has a higher affinity towards oxygen than “V.” Therefore, the possibility of an oxygen vacancy in the STO component of the LVO/STO heterostructure is much less in comparison with the STO component of a LAO/STO heterostructure and, hence, the use of  $\text{LaVO}_3$  instead of  $\text{LaAlO}_3$  as the film layer becomes important.

A fascinating topic with, however, patchy understanding is the distribution and origin of the conducting layer. It is reported that most conducting electrons are concentrated within a range of 7–10 nm near the interface on the STO side, although a long tail of the carrier density is extended up to 1  $\mu\text{m}$  [25–27]. Understanding carrier density distribution, the shape of the confinement potential and electronic subband quantization is getting increasing attention because of the possibility of the existence of “Rashba spin-splitting” bands in the 2DEG at the conducting interface of perovskite oxides [17,18,28–30]. It is now crucially important to amplify the shape of the confinement potential that may produce an internal electric field at the interface. The electric field produced at the interface transforms in the rest frame of a relativistic electron to a magnetic field that couples to its spin leading to a substantial Rashba spin-split band. In this Letter, we map the depth profile of conducting carriers at the interface of LVO and STO from room-temperature photoluminescence (PL) lifetime measurements. From a theoretical model, we determine the shape of the confinement potential well and the energy subbands at the interface. Using the theoretical model and the PL lifetime data, we estimate the carrier density and effective masses of the conducting electrons, which match rather well with those obtained from electric transport measurements. The LVO/STO heterostructure was grown by a pulsed laser deposition system using a  $\text{LaVO}_4$  polycrystalline ceramic pellet as a target. The KrF laser of the fluence of 2  $\text{J cm}^{-2}$  at a repetition rate of 2 Hz was used to ablate the target, and 150 nm of the LVO thin film was deposited on top of the  $\text{TiO}_2$  terminated (001) STO at 600 °C in  $1 \times 10^{-6}$ -Torr oxygen partial pressure [17,31]. The schematic of the heterostructure is shown in Fig. 1(a). The resistivity of the interface is measured as a function of temperature which suggests a metallic nature of the interface down to 3 K [see Fig. 1(b)]. To measure the resistivity of the system, we had used an ultrasonic wire bonder to connect the measurement systems to the interface. We have checked the top-down conductivity of the system and found it is electrically insulating within our measurement limit. We have also ensured that the film is insulating. It is worth mentioning that below around 5 K there is small upturn in the resistance. A similar effect reported by Hotta *et al.* and was explained by the localization mechanism arising from the defects present in the system [31,32]. We first focus our attention on Fig. 1(c) which shows the PL spectra of an undoped STO single crystal and a  $n$ -type LVO/STO heterostructure

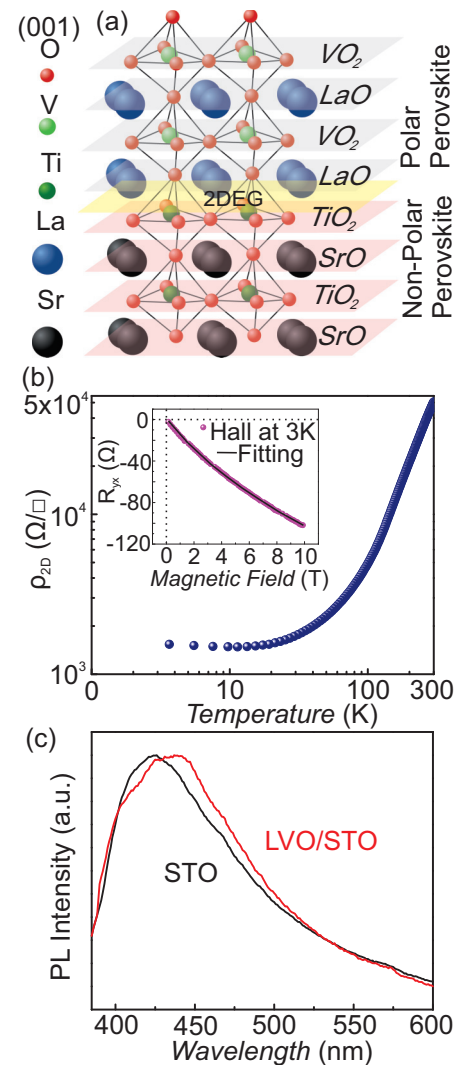


FIG. 1. (a) Schematic of the LVO/STO heterostructure showing the alternative charged layers of LVO and neutral layers of STO that gives rise to 2DEG at the interface and (b) 2D resistivity of the LVO/STO sample. The inset shows the low-temperature (3-K) Hall measurement, and (c) shows the room-temperature PL measurement of the undoped (001) STO single crystal and the LVO/STO heterostructure.

at room temperature. The excitation photon energy and the excitation density used is 3.54 eV and 0.028  $\text{mJ/cm}^2$ , respectively. The PL peak is at 2.9 eV for the undoped STO whereas the LVO/STO heterostructure is characterized by a broad peak at 2.8 eV (blue PL) which is similar to the previously reported electron-doped  $\text{SrTi}_{1-x}\text{Nb}_x\text{O}_3$  and  $n$ -type LAO/STO heterostructures [27,33,34]. The broad PL peak for nondoped STO signifies the polaron (electron-phonon coupling) formation, defects states, or the impurity present in the system [35]. The origin of the similar broad peak in LVO/STO is, thus, mainly from the STO substrate. The blue PL observed for the LVO/STO heterostructure is because of the two-carrier radiative recombination of photogenerated electrons and the holes. The dynamics of photogenerated carrier density  $n(t)$  [or

$p(t)$ ] and the PL intensity  $I(t)$  are governed by the following rate equations [27,35,36]:

$$\frac{dn}{dt}(t) = -An(t) - B_{\text{rad}}n(t)p(t) - C[n^2(t)p(t) + p^2(t)n(t)], \quad (1)$$

$$I(t) \propto B_{\text{rad}}n(t)p(t). \quad (2)$$

Here  $A$ ,  $B_{\text{rad}}$ , and  $C$  are the nonradiative photogenerated single carrier (electron or hole) trapping rate, two-carrier radiative recombination coefficient, and nonradiative Auger recombination rate, respectively. The Auger recombination is a three-carrier (electron-electron-hole and hole-hole-electron) nonradiative recombination.

When we shine light on undoped STO, electrons and holes are generated. These photogenerated electrons and holes are identical ( $n(t) = p(t)$ , here  $n(t)[p(t)]$  represents the number density of electrons (holes) at time  $t$  in number. In the conducting LVO/STO interface the number of intrinsic electrons ( $N_e$ ) is much greater than that of the photogenerated electrons ( $N_e \gg n$ ;  $N_e + n \sim N_e$ ). It is reported that at room temperature the radiative recombination is very small for undoped STO [38]. The term “ $B_{\text{rad}}n(t)p(t)$ ” could be neglected from Eq. (1) as it is significantly small in comparison with the other two terms. This leads to the fact that the PL is dominated by the Auger recombination of doped electrons and photogenerated holes [27,34,35]. For the conducting LVO/STO interface, Eqs. (1) and (2) are now modified to (with the approximation:  $n^2(t)p(t) + p^2(t)n(t) = [N_e + n(t)]^2 p(t) + p^2(t)(N_e + n) \sim N_e^2 p(t) + p^2(t)N_e$ : for  $N_e \gg n$ ),

$$\frac{dp}{dt}(t) = -Ap(t) - CN_e^2 p(t), \quad N_e \gg n. \quad (3a)$$

Integrating both sides of Eq. (3a) we get

$$p(t) = \exp -(A + CN_e^2)t, \quad (3b)$$

$$I(t) \propto B_{\text{rad}}N_e p(t). \quad (4)$$

From Eq. (3b), the photogenerated carrier/hole decay is exponential with decay rate  $(A + CN_e^2)$ . The photogenerated carrier/hole decay rate is dependent on the intrinsic carrier density. In addition, the PL decay has a direct relationship with the photogenerated carrier decay [Eq. (4)], hence, the intrinsic carrier density of the sample can be calculated using PL decay. The optical penetration depth is very sensitive to the excitation wavelength of the used laser [37]. The penetration depth for the laser 375 and 405 nm is  $\sim 300$  nm and  $> 10$   $\mu\text{m}$ , respectively, hence, by using laser 375 nm, electron dynamics around 100 nm below the interface can satisfactorily be monitored, and the laser 405 nm is monitoring the bulk of the sample [27,37].

Figures 2(a) and 2(b) represent the PL dynamics of the undoped (001) STO and the LVO/STO heterostructure for different excitation wavelengths (375 and 405 nm) monitored at 2.9 and 2.8 eV, respectively. It can be clearly seen from Figs. 2(a) and 2(b) that the PL decay rate for undoped STO is slower than that of the LVO/STO interface. The decay rate of nondoped STO at 405 nm is slower than at 375 nm and signifies the low carrier density in the bulk of the sample

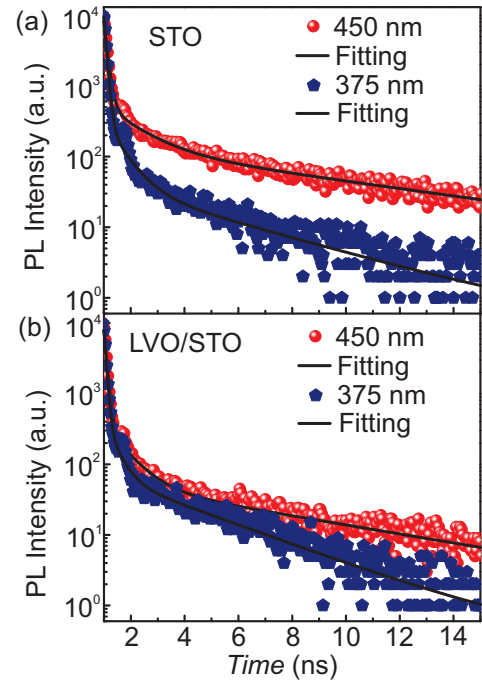


FIG. 2. PL dynamics of (a) undoped STO and (b) a LVO/STO heterostructure under the excitation wavelengths of 375 and 405 nm monitored at 426 and 442 nm, respectively. The solid curves represent the theoretical fitting of PL dynamics using Eq. (6).

in comparison to the surface. A similar behavior is already reported that shows a nonexponential behavior and explained in terms of the inhomogeneous distribution of carriers in the nondoped STO [38]. The faster decay in the LVO/STO heterostructure is due to the Auger recombination of the 2DEG originated at the interface and the photogenerated holes [34,38,39]. From Fig. 2(b), a nonexponential behavior of the PL decay curve in the LVO/STO sample is observed, which suggests that the charge carriers near the interface are inhomogeneously distributed in space. The decay rate is faster for the lower excitation (375-nm) wavelength corresponding to the least penetration of light, suggesting that most of the carriers are accumulated at the interface of the LVO/STO heterostructure. We have tabulated the decay constants of bare STO and the LVO/STO interface for both 405 and 375 nm light in (the Supplemental Material part (3), Table 1 [40]).

From Eq. (4) the temporal variation of the PL intensity is given by

$$I(t) \propto B_{\text{rad}} \int_0^{\infty} N_e(z)p(z,t)dz. \quad (5)$$

Here,  $p(z,t)$  is calculated from Eq. (3a),  $p(z,0) = p_0 \exp(-\alpha z)$ , where  $1/\alpha$  is defined as the optical penetration depth. To solve Eq. (5) we have used  $N_e(z) = N_0 \exp(-\beta z)$ , where  $1/\beta$  is the depth of the carrier distribution as the spatial distribution of the charge should be a smooth function of the distance that will decrease as you go away from the interface. The simplest and obvious choice is an exponential dependence. The previous reports have also used an exponential special variation of charge [27,35,38,41].

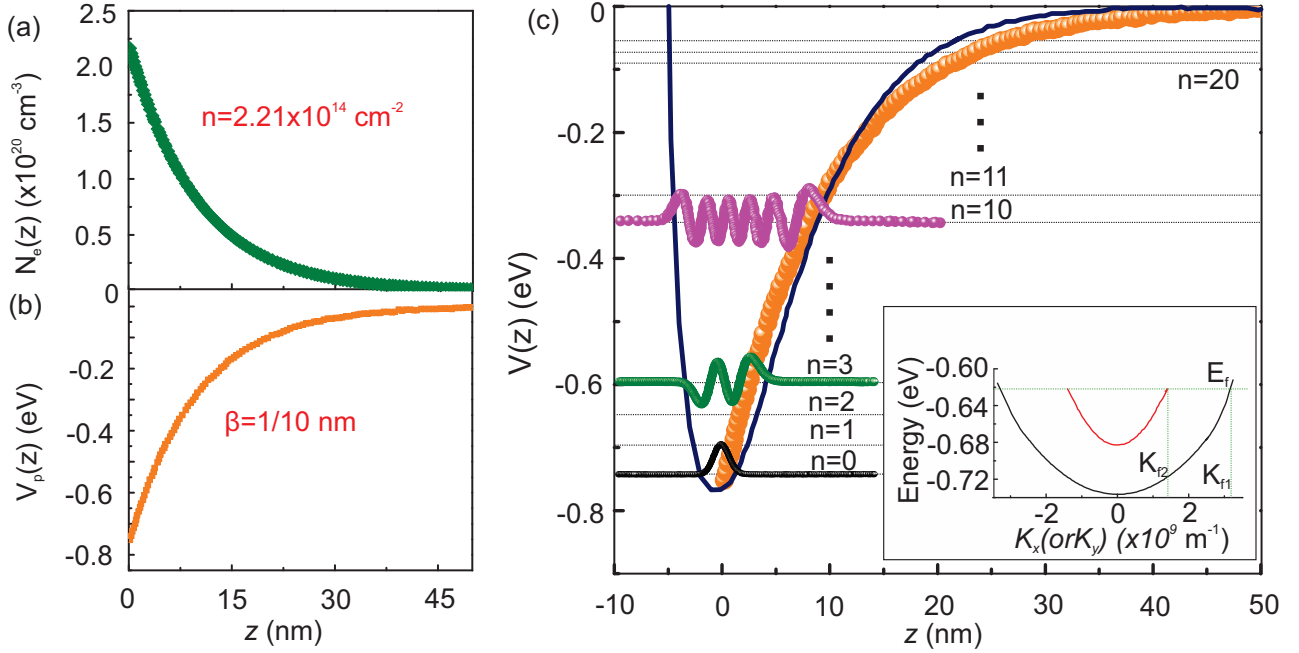


FIG. 3. (a) Calculated spatial profile of the carriers at the interface perpendicular to the surface, (b) calculated potential energy as a function of depth from the surface, and (c) the confinement potential  $V_P(Z)$  calculated from Poisson's equation and  $V_M(Z)$  the Morse potential as a function of depth ( $Z$ ) from the interface ( $Z = 0$ ,  $Z > 0$  is the STO side and  $Z < 0$  is the LVO side). The dotted lines show the energy subbands of the potential well with the calculated wave function for the given energy level, and the inset represents the projection of the same in  $K_x$  (or the  $K_y$ )- $E$  plane, the two Fermi momentum vectors corresponding to two conducting channels as well as the Fermi level are also indicated.

By substituting all values in Eq. (5) we get the PL intensity as

$$I(t) \propto \frac{K}{\beta} e^{-At} [1 - \text{erf}(N_0 \sqrt{Ct})], \quad (6)$$

where,  $\text{erf}(N_0 \sqrt{Ct})$  is an error function of its argument. The values of the constants  $A = 1.7 \times 10^6 \text{ s}^{-1}$  and  $C = 1.3 \times 10^{-32} \text{ cm}^6 \text{ s}^{-1}$  are taken from the previously calculated values for undoped STO [34,38,39]. The existence of surface carriers in nondoped STO is already reported with a typical value of  $N_0 \sim 10^{18} \text{ cm}^{-3}$  [34,38,42]. The  $N_0$  obtained from our fitting of nondoped STO data [Fig. 2(a)] is  $\sim 1.07 \times 10^{18} \text{ cm}^{-3}$  and is in good agreement with previous reports. To estimate the value of  $N_0$  and  $1/\beta$  for the LVO-STO interface we have fitted the experimental data of Fig. 2(b). The best fit is obtained as  $1/\beta = 10 \text{ nm}$  and  $N_0 = 2.21 \times 10^{20} \text{ cm}^{-3}$  for the LVO-STO sample [Fig. 2(b)] for which the total carrier density obtained from the spatial integration of  $N_e(Z)$  is ensured to match well with that obtained from Hall measurements. The potential-energy profile [ $V_P(z)$ ] near the interface as a function of depth is calculated from Poisson's equation given as [43]

$$V_P(z) = -\frac{eN_0}{\epsilon(0)\epsilon_0} \left( \frac{e^{-\beta z}}{\beta^2} \right), \quad (7)$$

and is drawn in Fig. 3(b). As it turns out, the potential distribution can be well approximated by the Morse potential [ $V_M(z)$ ] [44],

$$V_M(z) = D_e (e^{-2a(z)} - 2e^{-a(z)}), \quad (8)$$

where,  $D_e$  represents the depth of the potential well. The value of the  $\epsilon$  used in Eq. (7) is 400. In Eq. (8),  $a$  represents

the width of the potential well formed at the interface ( $a = 1/\beta = 10 \text{ nm}$ ). Figure 3(c) shows the potential-energy profile generated from the Poisson relation Eq. (7) and the Morse potential Eq. (8). The eigenvalues and eigenfunctions of the Morse potential are exactly solvable [45]. This fact is utilized to find out the energy eigenvalue and the wave function for this confinement potential by using the Morse potential approximation. The calculated energy eigenvalues and wave function for the LVO/STO system are shown in Fig. 3(c). To calculate the energy eigenvalues, we have used the effective mass of STO  $1.5m_e$ . The wave function quickly vanishes as we go away from the interface especially for lower subbands. The spatial distribution of the intrinsic carrier as a function of depth from the interface is plotted in Fig. 3(a) which indicates that most of the intrinsic conducting carriers are concentrated within a few nanometers near the LVO/STO interface. The total calculated carrier density  $\sim 2.21 \times 10^{14} \text{ cm}^{-2}$  is very close to the carrier density ( $3 \times 10^{14} \text{ cm}^{-2}$ ) predicted from the polar catastrophe model [46]. A similar carrier density also may be obtained in oxygen vacant STO-based interfaces. But in the present case, we have ensured that the level of oxygen vacancy in the present system is below the detection limit and, hence, extremely low.

The Hall measurement was performed to elicit the nature and amount of the charge carrier present in the system. We have applied current along the  $x$  axis, a magnetic field is applied along the  $z$  axis, and the Hall resistance is measured. The sign of the Hall resistance suggests that the carriers are of  $n$  type. The inset of Fig. 1(b) shows the Hall data at 3 K, having a nonlinear nature. Similar nonlinear behavior was also reported previously for the LVO/STO interface [31,32].



This nonlinear nature of the curve indicates the presence of two types of electrons and, hence, the existence of two-band conduction in this system [32,47,48]. In the two-band model, two conduction channels are corresponding to two groups of charge carriers with mobilities  $\mu_1$  and  $\mu_2$  and charge carrier densities  $n_1$  and  $n_2$ . In the two-band model, the Hall and longitudinal resistances are written as

$$R_{xy}(B) = \frac{B}{e} \frac{n_1\mu_1^2 + n_2\mu_2^2 + (n_1 + n_2)(\mu_1\mu_2B)^2}{(n_1\mu_1 + n_2\mu_2)^2 + (n_1 + n_2)^2(\mu_1\mu_2B)^2}. \quad (9)$$

This equation has four unknown parameters but could be rewritten as an effective two-free parameter equation by using the fact the longitudinal resistance ( $R_{xx}$ ) in the absence of any applied magnetic field is given by

$$R_{xx}(B = 0) = \frac{1}{e(n_1\mu_1 + n_2\mu_2)}. \quad (10)$$

The best fit is for carrier densities  $n_1 = 0.54 \times 10^{14}$  and  $n_2 = 1.7 \times 10^{14} \text{ cm}^{-2}$  with mobility values of  $\mu_1 = 500$  and  $\mu_2 = 2000 \text{ cm}^2 \text{ V}^{-1} \text{ s}^{-1}$ , respectively. A detailed description of this analysis is given in Ref. [32]. The effective masses for the energy subband calculated from these data are  $2.1m_e$  and  $0.67m_e$ . The effective masses are calculated from the mobility by using scattering time  $7 \times 10^{-13} \text{ s}$  [49–51]. The effective mass of the carriers is similar to that reported for LAO/STO systems ( $\sim 2.5m_e$  and  $\sim 0.5m_e$ ) [50,52–54].

We have adopted the following scheme to draw the electronic bands [Fig. 3(c) inset] of this system. From the two-band fitting of Hall data, the carrier density of the individual conducting channel was calculated. By using the mass of the majority carriers the curvature of that parabolic band was determined, and the carrier density was used to find out the Fermi velocity and the Fermi level of the system. Keeping the Fermi level fixed for the second conduction channel and estimating the Fermi velocity from the carrier density of the minority carrier, the second parabolic band is drawn. For both channels the energy value at  $K = 0$  is determined by the energy eigenvalue estimated from confinement potential. It is pleasantly surprising to note that the effective mass of the second channel ( $m_2^* = 0.6m_e$ ) matches excellently with that estimated from the Hall measurement ( $m_2^* = 0.67m_e$ ). The parabolas in the Fig. 3(c) inset represent the two types of carriers, namely, light and heavy carriers. This is very similar to the Ti  $3d$   $t_{2g}$  band splitting in the STO at the interface of the LAO/STO heterostructure [55,56].

In conclusion, we have proposed a method to map out the carrier density distribution, the quantum well structure, and the related energy subbands for a conducting interface by combining the optical spectroscopy with the electrical transport measurements utilizing a theoretical model. Our experiments on the conducting interface of LVO/STO suggest that the potential near the interface could be well approximated by the Morse potential. It is also important to note that the distribution of the carriers is mostly concentrated within a few nanometers near the LVO/STO interface, suggesting a nearly two-dimensional nature of this electronic system. This confinement leads to the formation of electronic subbands. The wave function and the energy subbands for this quantum well are analytically solved with the Morse potential approximation. The total carrier density estimated from this carrier density distribution is  $2.21 \times 10^{14} \text{ cm}^{-2}$ , which is very close to the carrier density of  $\sim 3 \times 10^{14} \text{ cm}^{-2}$  predicted from the polar catastrophe model and the one deduced by analyzing the Hall data. By fitting the observed nonlinear Hall data with the two-band theory the mobility for two conducting channels are estimated to 500 and  $2000 \text{ cm}^2 \text{ V}^{-1} \text{ s}^{-1}$ . The corresponding carrier densities are  $0.54 \times 10^{14}$  and  $1.7 \times 10^{14} \text{ cm}^{-2}$ , respectively. Excellent agreement in the effective masses estimated from electrical transport measurements ( $m_1^*: 2.1m_e$  and  $m_2^*: 0.67m_e$ ) and optical spectroscopies ( $m_1^*: 2m_e$  and  $m_2^*: 0.6m_e$ ) have been observed. Our method offers a way to examine the electronic distribution, shape of the confinement potential, as well as the electronic structure of a conducting interface. This method is not restricted to any particular system and could be extended to other conducting interfaces as well. A fair understanding of the quantum well and related energy subband structure might be helpful to understand recently observed fascinating physical properties arising from the ‘‘Rashba interaction,’’ such as the planar Hall effect, the nontrivial Berry phase, etc., at the conducting oxide interfaces with strong spin-orbit coupling.

#### ACKNOWLEDGMENTS

S.D. is grateful to the Indian National Science Academy for its support through their Senior Scientist Scheme. This project was supported by Grant No. 58/14/17/2019-BRNS/37024 (BRNS). Conflict of Interest: The authors declare no conflict of interest.

- [1] A. M. Voshchenkov and J. N. Zemel, Admittance studies of surface quantization in [100]-oriented Si metal-oxide-semiconductor field-effect transistors, *Phys. Rev. B* **9**, 4410 (1974).
- [2] D. Zanato, S. Gokden, N. Balkan, B. K. Ridley, and W. J. Schaff, The effect of interface-roughness and dislocation scattering on low temperature mobility of 2D electron gas in GaN/AlGaN, *Semicond. Sci. Technol.* **19**, 427 (2004).
- [3] A. Ohtomo and H. Y. Hwang, A high-mobility electron gas at the LaAlO<sub>3</sub>/SrTiO<sub>3</sub> heterointerface, *Nature (London)* **427**, 423 (2004).

- [4] C. W. Bark, P. Sharma, Y. Wang, S. H. Baek, S. Lee, S. Ryu, C. M. Folkman, T. R. Paudel, A. Kumar, S. V. Kalinin, A. Sokolov, E. Y. Tsymbal, M. S. Rzchowski, A. Gruverman, and C. B. Eom, Switchable induced polarization in LaAlO<sub>3</sub>/SrTiO<sub>3</sub> heterostructures, *Nano. Lett.* **12**, 1765 (2012).
- [5] M. Caputo, M. Boselli, A. Filippetti, S. Lemal, D. Li, A. Chikina, C. Cancellieri, T. Schmitt, J. M. Triscone, P. Ghosez, S. Gariglio, and V. N. Strocov, Artificial quantum confinement in LaAlO<sub>3</sub>/SrTiO<sub>3</sub> heterostructures, *Phys. Rev. Materials* **4**, 035001 (2020).

- [6] N. Reyren, S. Thiel, A. D. Caviglia, L. F. Kourkoutis, G. Hammerl, C. Richter, C. W. Schneider, T. Kopp, A. S. Rüetschi, D. Jaccard, M. Gabay, D. A. Muller, J. M. Triscone, and J. Mannhart, Superconducting interfaces between insulating oxides, *Science* **317**, 1196 (2007).
- [7] S. Gariglio, N. Reyren, A. D. Caviglia, and J. M. Triscone, Superconductivity at the LaAlO<sub>3</sub>/SrTiO<sub>3</sub> interface, *J. Phys.: Condens. Matter* **21**, 16 (2009).
- [8] K. S. Takahashi, M. Kawasaki, and Y. Tokura, Interface ferromagnetism in oxide superlattices of CaMnO<sub>3</sub>/CaRuO<sub>3</sub>, *Appl. Phys. Lett.* **79**, 1324 (2001).
- [9] L. Li, C. Richter, J. Mannhart, and R. C. Ashoori, Coexistence of magnetic order and two-dimensional superconductivity at LaAlO<sub>3</sub>/SrTiO<sub>3</sub> interfaces, *Nat. Phys.* **7**, 762 (2011).
- [10] T. F. Nova, A. S. Disa, M. Fechner, and A. Cavalleri, Metastable ferroelectricity in optically strained SrTiO<sub>3</sub>, *Science* **364**, 1075 (2018).
- [11] J. B. N. J. Wang, J. B. Neaton, H. Zheng, V. Nagarajan, S. B. Ogale, B. Liu, D. Viehland, V. Vaithyanathan, D. G. Schlom, and U. V. Waghmare, Epitaxial BiFeO<sub>3</sub> multiferroic thin film heterostructures, *Science* **299**, 1719 (2003).
- [12] R. Ramesh and N. A. Spaldin, Multiferroics: Progress and prospects in thin films, *Nat. Mater.* **6**, 21 (2007).
- [13] M. C. Tarun, F. A. Selim, and M. D. McCluskey, Persistent Photoconductivity in Strontium Titanate, *Phys. Rev. Lett.* **111**, 187403 (2013).
- [14] S. Goyal, N. Wadehra, and S. Chakraverty, Tuning the electrical state of 2DEG at LaVO<sub>3</sub>-KTaO<sub>3</sub> interface: Effect of light and electrostatic gate, *Adv. Mater. Interfaces* **7**, 2000646 (2020).
- [15] S. Goyal, A. Singh, R. Tomar, R. Kaur, C. Bera, and S. Chakraverty, Persistent photoconductivity at LaVO<sub>3</sub>-SrTiO<sub>3</sub> interface, *Solid State Commun.* **316**, 113930 (2020).
- [16] T. Tsuyama, S. Chakraverty, S. Macke, N. Pontius, C. Schüßler-Langeheine, H. Y. Hwang, Y. Tokura, and H. Wadati, Photoinduced Demagnetization and Insulator-to-Metal Transition in Ferromagnetic Insulating BaFeO<sub>3</sub> thin films, *Phys. Rev. Lett.* **116**, 256402 (2016).
- [17] N. Wadehra, R. Tomar, R. M. Varma, R. K. Gopal, Y. Singh, S. Dattagupta, and S. Chakraverty, Planar Hall effect and anisotropic magnetoresistance in polar-polar interface of LaVO<sub>3</sub>-KTaO<sub>3</sub> with strong spin-orbit coupling, *Nat. Commun.* **11**, 874 (2020).
- [18] N. Kumar, N. Wadehra, R. Tomar, S. Dattagupta, S. Kumar, and S. Chakraverty, Observation of Shubnikov-de Haas oscillations, planar Hall effect, and anisotropic magnetoresistance at the conducting interface of EuO-KTaO<sub>3</sub>, *Adv. Quantum Technol.* **4**, 2000081 (2020).
- [19] J. Mannhart, and D. G. Schlom, Oxide interfaces—an opportunity for electronics, *Science* **327**, 1607 (2010).
- [20] L. Chen, E. Sutton, H. Lee, J.-W. Lee, J. Li, Ch.-B. Eom, P. Irvin, and J. Levy, Over 100-THz bandwidth selective difference frequency generation at LaAlO<sub>3</sub>/SrTiO<sub>3</sub> nanojunctions, *Light: Sci. Appl.* **8**, 24 (2019).
- [21] Y. Tokura and N. Nagaosa, Emergent functions of quantum materials, *Nat. Phys.* **13**, 1056 (2017).
- [22] H. Y. Hwang, Y. Iwasa, M. Kawasaki, B. Keimer, N. Nagaosa, and Y. Tokura, Emergent phenomena at oxide interfaces, *Nature Mater.* **11**, 103 (2012).
- [23] H. Banerjee, S. Banerjee, M. Randeria, and T. Saha-Dasgupta, Electronic structure of oxide interfaces: A comparative analysis of GdTiO<sub>3</sub>/SrTiO<sub>3</sub> and LaAlO<sub>3</sub>/SrTiO<sub>3</sub> interfaces, *Sci. Rep.* **5**, 1 (2015).
- [24] R. Tomar, S. Kakkar, C. Bera, and S. Chakraverty, Anisotropic magnetoresistance and planar Hall effect in (001) and (111) LaVO<sub>3</sub>/SrTiO<sub>3</sub> heterostructures, *Phys. Rev. B* **103**, 115407 (2021).
- [25] M. Basletic, J. L. Maurice, C. Carrétéro, G. Herranz, O. Copie, M. Bibes, E. Jacquet, and K. Bouzouhane, Mapping the spatial distribution of charge carriers in LaAlO<sub>3</sub>/SrTiO<sub>3</sub> heterostructures, *Nature (London)* **7**, 621 (2008).
- [26] N. Reyren, S. Gariglio, A. D. Caviglia, D. Jaccard, T. Schneider, and J. M. Triscone, Anisotropy of the superconducting transport properties of the LaAlO<sub>3</sub>/SrTiO<sub>3</sub> interface, *Appl. Phys. Lett.* **94**, 112506 (2009).
- [27] Y. Yamada, H. K. Sato, Y. Hikita, H. Y. Hwang, and Y. Kanemitsu, Spatial density profile of electrons near the LaAlO<sub>3</sub>/SrTiO<sub>3</sub> heterointerface revealed by time-resolved photoluminescence spectroscopy, *Appl. Phys. Lett.* **104**, 151907 (2014).
- [28] H. Zhang, H. R. Zhang, X. Yan, X. J. Zhang, Q. H. Zhang, J. Zhang, F. R. Han, L. Gu, B. G. Liu, Y. S. Chen, B. S. Shen, and J. R. Sun, Highly mobile two-dimensional electron gases with a strong gating effect at the amorphous LaAlO<sub>3</sub>/KTaO<sub>3</sub> interface, *ACS Appl. Mater. Interfaces* **9**, 36456 (2017).
- [29] K. Zou, S. Ismail-Beigi, K. Kisslinger, X. Shen, D. Su, F. J. Walker, and C. H. Ahn, LaTiO<sub>3</sub>/KTaO<sub>3</sub> interfaces: A new two-dimensional electron gas system, *APL Mater.* **3**, 036104 (2015).
- [30] H. Zhang, Y. Yun, X. Zhang, H. Zhang, Y. Ma, X. Yan, F. Wang, G. Li, R. Li, T. Khan *et al.*, High-Mobility Spin-Polarized Two-Dimensional Electron Gases at EuO/KTaO<sub>3</sub> Interfaces, *Phys. Rev. Lett.* **121**, 116803 (2018).
- [31] Y. Hotta, T. Susaki, and H. Y. Hwang, Polar Discontinuity Doping of the LaVO<sub>3</sub>/SrTiO<sub>3</sub> Interface, *Phys. Rev. Lett.* **99**, 236805 (2007).
- [32] H. Rotella, O. Copie, A. Pautrat, P. Boullay, A. David, D. Pelloquin, C. Labbe, C. Frilay, and W. Prellier, Two components for one resistivity in LaVO<sub>3</sub>/SrTiO<sub>3</sub> heterostructure, *J. Phys.: Condens. Matter* **27**, 095603 (2015).
- [33] S. Cook, M. T. Dylla, R. A. Rosenberg, Z. R. Mansley, G. J. Snyder, L. D. Marks, and D. D. Fong, The Vacancy-Induced Electronic Structure of the SrTiO<sub>3-δ</sub> Surface, *Adv. Electron. Mater.* **5**, 1800460 (2019).
- [34] Y. Yamada, H. Yasuda, T. Tayagaki, and Y. Kanemitsu, Temperature Dependence of Photoluminescence Spectra of Nondoped and Electron-Doped SrTiO<sub>3</sub>: Crossover from Auger Recombination to Single-Carrier Trapping, *Phys. Rev. Lett.* **102**, 247401 (2009).
- [35] H. Yasuda and Y. Kanemitsu, Dynamics of nonlinear blue photoluminescence and Auger recombination in SrTiO<sub>3</sub>, *Phys. Rev. B* **77**, 193202 (2008).
- [36] G. Leising, *Recombination in Semiconductors*, edited by P. T. Landsberg (Cambridge University Press, Cambridge, 1991), 595 pp.
- [37] M. Cardona, Optical Properties and Band Structure of SrTiO<sub>3</sub> and BaTiO<sub>3</sub>, *Phys. Rev.* **140**, A651 (1965).
- [38] H. Yasuda, Y. Yamada, T. Tayagaki, and Y. Kanemitsu, Spatial distribution of carriers in SrTiO<sub>3</sub> revealed by photoluminescence dynamics measurements, *Phys. Rev. B* **78**, 233202 (2008).

- [39] Y. Yamada, H. Yasuda, T. Tayagaki, and Y. Kanemitsu, Photocurrent recombination dynamics in highly excited SrTiO<sub>3</sub> studied by transient absorption and photoluminescence spectroscopy, *Appl. Phys. Lett.* **95**, 121112 (2009).
- [40] See Supplemental Material at <https://link.aps.org/supplemental/10.1103/PhysRevB.104.L081111>, which includes Refs. [27,34,36,38], for details of equation and fitting parameters used in the paper.
- [41] R. Tomar, R. M. Varma, N. Kumar, D. D. Sarma, D. Maryenko, and S. Chakraverty, Conducting LaVO<sub>3</sub>/SrTiO<sub>3</sub> Interface: Is Cationic Stoichiometry Mandatory?, *Adv. Mater. Interfaces* **7**, 1900941 (2020).
- [42] A. F. Santander-Syro, O. Copie, T. Kondo, F. Fortuna, S. Pailhes, R. Weht, X. G. Qiu, F. Bertran, A. Nicolaou, and A. Taleb-Ibrahimi, Two-dimensional electron gas with universal subbands at the surface of SrTiO<sub>3</sub>, *Nature (London)* **469**, 189 (2012).
- [43] W. Monch, *Semiconductor Surfaces and Interfaces* (Springer, Berlin, 2001).
- [44] P. Y. Myatt, A. K. Dham, P. Chandrasekhar, F. R. W. McCourt, and R. J. Le Roy, A new empirical potential energy function for Ar<sub>2</sub>, *Mol. Phys.* **116**, 1598 (2018).
- [45] M. H. Hulburt and J. O. Hirschfelder, Potential energy functions for diatomic molecules, *J. Chem. Phys.* **9**, 61 (1941).
- [46] A. Savoia, D. Paparo, P. Perna, Z. Ristic, M. Salluzzo, F. Miletto Granozio, U. Scotti di Uccio *et al.*, Polar catastrophe and electronic reconstructions at the LaAlO<sub>3</sub>/SrTiO<sub>3</sub> interface: Evidence from optical second harmonic generation, *Phys. Rev. B* **80**, 075110 (2009).
- [47] C. Bell, S. Harashima, Y. Kozuka, M. Kim, B. G. Kim, Y. Hikita, and H. Y. Hwang, Dominant Mobility Modulation by the Electric Field Effect at the LaAlO<sub>3</sub>/SrTiO<sub>3</sub> Interface, *Phys. Rev. Lett.* **103**, 226802 (2009).
- [48] J. S. Kim, S. S. A. Seo, M. F. Chisholm, R. K. Kremer, H.-U. Habermeier, B. Keimer, and H. N. Lee, Nonlinear Hall effect and multichannel conduction in LaTiO<sub>3</sub>/SrTiO<sub>3</sub> superlattices, *Phys. Rev. B* **82**, 201407(R) (2010).
- [49] A. Fete, S. Gariglio, A. D. Caviglia, J. M. Triscone, and M. Gabay, Rashba induced magnetoconductance oscillations in the LaAlO<sub>3</sub>-SrTiO<sub>3</sub> heterostructure, *Phys. Rev. B* **86**, 201105(R) (2012).
- [50] M. Ben Shalom, A. Ron, A. Palevski, and Y. Dagan, Shubnikov-de Haas Oscillations in SrTiO<sub>3</sub>/LaAlO<sub>3</sub> Interface, *Phys. Rev. Lett.* **105**, 206401(R) (2010).
- [51] N. Kumar *et al.*, have calculated the relaxation time of STO at 2 K is  $\sim 8 \times 10^{-13}$  s, using deformation potential and rigid band approximation (unpublished).
- [52] W. J. Son, E. Cho, B. Lee, J. Lee, and S. Han, Density and spatial distribution of charge carriers in the intrinsic n-type LaAlO<sub>3</sub>-SrTiO<sub>3</sub> interface, *Phys. Rev. B* **79**, 245411 (2009).
- [53] A. Fete, S. Gariglio, C. Berthod, D. Li, D. Stornaiuolo, M. Gabay, and J. M. Triscone, Large modulation of the Shubnikov-de Haas oscillations by the Rashba interaction at the LaAlO<sub>3</sub>/SrTiO<sub>3</sub> interface, *New J. Phys.* **16**, 112002 (2014).
- [54] A. Fete, C. Cancellieri, D. Li, D. Stornaiuolo, A. D. Caviglia, S. Gariglio, and J. M. Triscone, Growth-induced electron mobility enhancement at the LaAlO<sub>3</sub>/SrTiO<sub>3</sub> interface, *Appl. Phys. Lett.* **106**, 051604 (2015).
- [55] M. Salluzzo, J. C. Cezar, N. B. Brookes, V. Bisogni, G. M. De Luca, C. Richter, S. Thiel, J. Mannhart, M. Huijben, A. Brinkman *et al.*, Orbital Reconstruction and the Two-Dimensional Electron Gas at the LaAlO<sub>3</sub>/SrTiO<sub>3</sub> Interface, *Phys. Rev. Lett.* **102**, 166804 (2009).
- [56] Z. S. Popović, S. Satpathy, and R. M. Martin, Origin of the Two-Dimensional Electron Gas Carrier Density at the LaAlO<sub>3</sub> on SrTiO<sub>3</sub> Interface, *Phys. Rev. Lett.* **101**, 256801 (2008).